Predicting the future: Predictive control for astronomical adaptive optics

Kooten M.A.M. van

Author: Kooten, M.A.M. van
Title: Predicting the future: Predictive control for astronomical adaptive optics
Issue Date: 2020-11-04

Chapter 1

Introduction

> "The wide world is all about you: you can fence yourselves in, but you cannot for ever fence it out."
>
> J.R.R. Tolkien, *The Fellowship of the Ring*

Giordano Bruno in the 16th century wrote "this space we declare to be infinite... in it are an infinity of worlds of the same kind as our own". Even with these early speculations on the existence of earth-like planets, it was not until the late 1980s that the first signs of a scientific detection of an exoplanet was made by Campbell et al. (1988). Unable to rule out intrinsic stellar variations as the source of the Doppler shifting in the observer radial velocity measurements of Gamma Cephei A., the confirmation of the exoplanet came later by Hatzes et al. (2003). The search for the first detection of an exoplanet continued until Wolszczan and Frail (1992) discovered variations in the period of a pulsar (i.e., pulsar timing method), using the Arecibo radio telescope, revealing two earth-sized planets orbiting a rotating neutron star. Shortly thereafter, 51 Pegasi b was indirectly detected at Haute-Provence Observatory by Mayor and Queloz (1995). The radial velocity measurements revealed a 4 day period hot Jupiter orbiting a main sequence star. Within a relatively short period of time, thousands of detections were subsequently made using primary radial velocity measurements and transit event detections, see Figure 1.1. With new and improved technology, the field of exoplanets has now moved from exoplanet detection to exoplanet characterisation. From a theoretical point of view, the discovery of a diverse population of exoplanets in different stages of their life-cycles, has made the fields of exoplanets and planet formation dynamic and rapidly evolving with many questions yet to be answered. Some of these questions include 1. how unique is our solar system, 2. how do planets form, and 3. is there life on other planets? To answer these questions, more in-depth studies of individual systems are needed for exoplanets in all stages of their evolution. This includes studying systems across a large portion of the electro-magnetic spectrum. Furthermore, the population sample of exoplanets must continue to increase to better understand planet formation and evolution, all the while trying to understand how the Solar System fits into these narratives. The rest of this introduction is dedicated to summarising current methods for detecting and characterising exoplanets; the tools that will help answer these fundamental questions. Specifically, we will explore the current challenges faced in directly imaging exoplanets and motivate the work that follows in this dissertation.

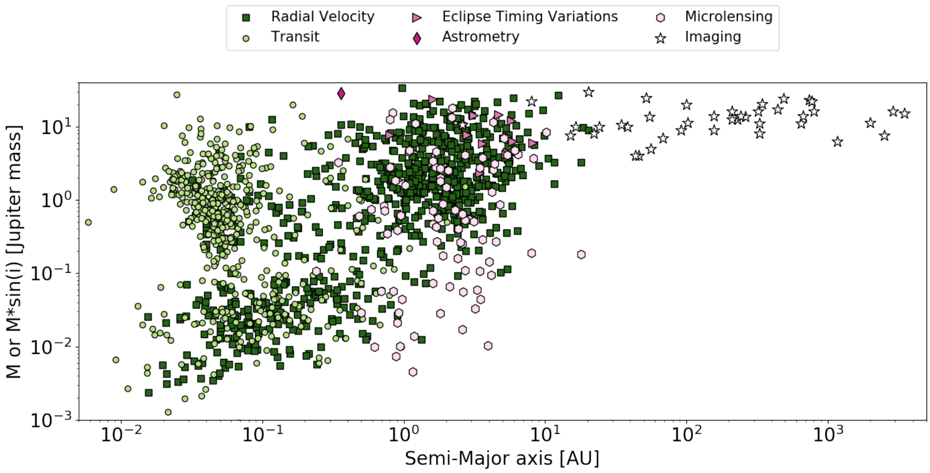

Figure 1.1: Mass or upper-mass limit ($Msin(i)$; for radial velocity only) of exoplanet candidates, sorted by discovery method, as a function of semi-major axis. Data NASA Exoplanet Archive accessed on 13/03/2020.

1.1 Indirect Methods for Detecting Exoplanets

Imaging exoplanets directly is a challenging task due to the required spatial resolution and contrast ($10^{-6} - 10^{-7}$ at separations of < 1 arc-seconds [symbol: "]). As a result, the majority of exoplanets are discovered with indirect techniques. Through indirect methods such as radial velocity measurements, transit photometry, and others (see summary of methods in Table 1.1), thousands of exoplanets have been detected, with their masses and/or radii estimated. Figure 1.1 provides a summary of current exoplanet candidates, categorised by the discovery method. In this section, we will briefly discuss indirect methods before taking an in-depth look at the direct imaging.

Radial Velocity

The radial velocity method—or Doppler spectroscopy—is a spectroscopic method for detecting exoplanets and binary star systems. It relies on taking series of spectra of a given star and finding periodic variations in the spectral time series that are not due to intrinsic stellar variations. The periodic signal is a result of a secondary body "pulling" on the primary body causing slight changes in position and therefore velocity as they orbit their centre of mass. By extracting the amplitude and period of the fluctuation as in Figure 1.2, information on the masses and orbital parameters of the system can be extracted. The method is, however, limited due to the lack of knowledge of the inclination, i, of the system, making it possible to only determine an upper mass limit.

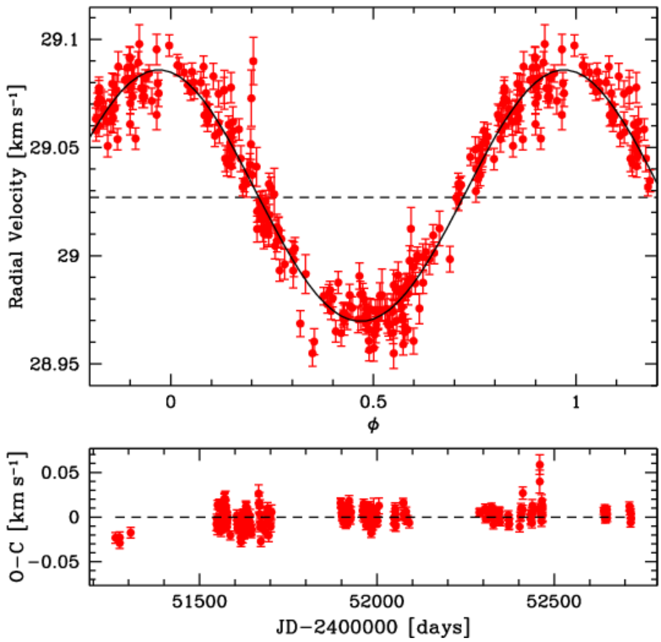

Figure 1.2: Radial velocity measurements (red) for HD 83443 as a function of folded phase with the best Keplerian planetary solution shown in solid. The bottom panel shows the residuals. Figure from Mayor, Udry, et al. (2004).

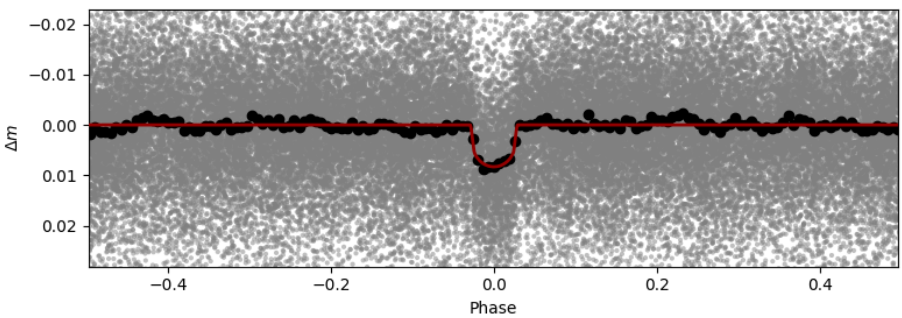

Figure 1.3: MASCARA light curve for the MASCARA-4b exoplanet. The grey points show all of the MASCARA data, while the solid black shows the averaged data. The red curve indicates the best fit. Figure from Dorval et al. (2020).

Table 1.1: Summary of the strengths and weaknesses of different exoplanet detection methods (based on Advanced School on Exoplanetary Science (1st : 2015 : Vietri sul Mare et al. (2016)).

Method	Strengths	Weaknesses
Radial velocity	As follow-up to transit events, allows for exoplanet confirmation; lower-limit mass estimation; get density estimation when combined with transit data	Sensitive to intrinsic stellar variability; bias towards larger close-in exoplanets
Transit photometry	Radius estimation; sensitive to multiple planets; atmosphere characteristics; easy for large surveys	Only sensitive to edge-on systems; measures relative radii; needs to capture multiple transit events; bias towards smaller semi-major-axis
Pulsar timing	Sensitive to all exoplanet masses for non-face-on systems	Very rare due to being a dead system
Microlensing	Sensitive to close-in, earth-like exoplanets	One-time events; unlikely to occur; degeneracies
Astrometry	Independent of stellar type and sensitive to all inclinations	More sensitive to larger, close-in exoplanets; needs well control systematics
Direct imaging	Direct measurement of thermal and/or reflected light; direct characterisation; does not require long baseline	Sensitive to face-on systems; bias towards young, large-separation exoplanets; bias toward nearby systems

Transit Photometry

Charbonneau, Brown, Latham, et al. (2000) detected the first transiting exoplanet, HD 209458b, and since then thousands of transiting exoplanet candidates have been discovered. The transiting method uses precision photometry of a given star over long periods of time. When a planet moves in front of the host star it blocks some of the emitted photons, resulting in a reduction of flux of the star as seen from the observer. The light curve—stellar flux as a function of time—of the recently discovered MASCARA-4b (Dorval et al., 2020) passing in front of its host star is shown in Figure 1.3. The light curve was taken by the Multi-site all-sky camera (MASCARA; Lesage et al. (2014)), a simple ground-based instrument looking for exoplanets with many locations around the world. With space-based telescopes such the

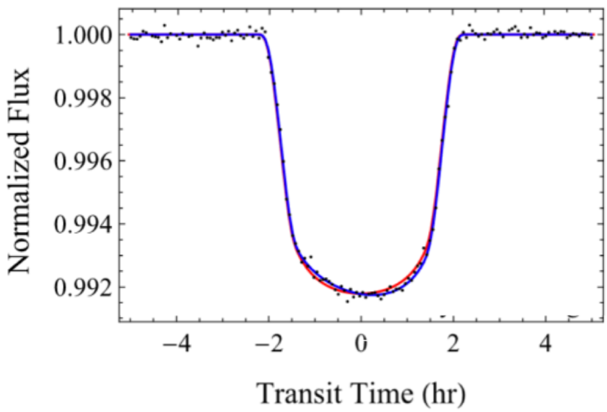

Figure 1.4: Light curve for MASCARA-4b as observed by TESS (black dots) with two different models of the exoplanet. Figure modified from Ahlers et al. (2020).

Kepler telescope (see Borucki et al., 2010) and its successor the Transiting Exoplanet Survey Satellite (TESS; Ricker et al. (2015)), the achievable photometric precision is much better compared to ground-based instruments, allowing the transiting method to discover planets with small radii and therefore relatively smaller masses as seen in Figure 1.1. Figure 1.4 shows the improvement in data quality with the light curve of Mascara-4b taken by TESS published by Ahlers et al. (2020). With telescopes such as Kepler, however, very bright stars are difficult to observe due to detector saturation. Ground-based observations from instruments such as MASCARA will therefore remain important.

The eclipse-timing variations (ETV) approach closely studies the periodicity of a transiting exoplanet, making use of many light curve measurements. In a great number of cases, slight variations in the timing of transits are observed. These variations often result from a transiting exoplanet experiencing the gravitational pull of another as-yet undetected planet, changing the time of the transits slightly. ETV is very effective in tightly packed planetary systems and is sensitive to earth-like masses.

When combined with measurements taken at different wavelengths, the light curve of an exoplanet can provide more information than just the radius and period of the exoplanet. Using transit spectroscopy at the start and end of each transit event (primary eclipse), the light from the host star that travels through the exoplanet's atmosphere can be measured. Some of the light will be absorbed by the atmosphere, allowing the chemical composition of the exoplanet's atmosphere to be inferred from the spectroscopic observation. When the exoplanet passes behind the host star (secondary eclipse), the thermal radiation and reflected light from the planet can be detected as it initially disappears and later reappears, providing information once again about the atmosphere of the exoplanet. Using the Hubble Space Telescope, Charbonneau, Brown, Noyes, et al. (2002) detected a dimming of sodium absorption during an exoplanet's transit, indicative of clouds on the exoplanet. Snellen et al. (2010) found evidence for winds in the upper atmosphere of HD 209458b from transit spectroscopy measurements of carbon monoxide. These discoveries and many others show the power of transit spectroscopy for exoplanet characterisation.

Beyond exoplanet detection

Transiting photometry not only allows for the discovery of exoplanets in an efficient way, but with large surveys such as Kepler, light curves can also be determined for every object in the field-of-view. With this type of data there is a very high potential to detect odd planetary systems that might look very different from what is expected along with signals not due to exoplanets at all. With new efforts to uncover them in archival data by Wheeler and Kipping (2019) and other groups that seek to find outlier signals, new knowledge on planet formation, disk dynamics, or stellar behaviour might be found. Specifically, the discovery of new brightening events in the Kepler data, leads me to ask **what type of astronomical objects could we be seeing in these newly found brightening events?**

1.2 High Contrast Imaging

Using an arsenal of different observing techniques the exoplanet community has primarily relied on indirect methods to detect the effects an exoplanet has on its host star, rather than directly observing the exoplanet itself. In the last 20 years, direct imaging has overcome previous technological barriers to allow for the imaging of the exoplanet itself in reflected light or thermal emission. High-contrast imaging (HCI) enables the direct imaging of exoplanets.

HCI systems image exoplanets by suppressing the light from the host star to reveal the faint exoplanet as shown in Figure 1.6. To date, HCI systems have reached post-processed contrasts of 10^{-6} at spatial separations of 200 milli-arc-second (mas) as determined by Zurlo et al. (2016). *Contrast* is defined as an object's flux compared to its host star's flux in terms of a specified signal-to-noise ratio (SNR). For post-processed images, the post-processed contrast is often defined using $SNR = 5$ or "5σ" detection. The performance of an HCI system is then given in terms of a contrast curve (contrast as a function of radial distance from the centre of the point-spread-function, psf). Since the first HCI detection, 3 exoplanets orbiting HR8799 by Marois, Macintosh, et al. (2008), many large, far out exoplanets have been discovered as shown in Figure 1.1. The orbital periods of the exoplanets around HR8799 range from 45–100 years while the orbital periods of exoplanets, such as 51 Pegasi b mentioned above, are on the order of days. These examples clearly show the different regimes that the methods operate within. HCI systems have also discovered protoplanetary, and circumstellar disks (e.g., Avenhaus et al., 2018; Sissa et al., 2018). By combining direct imaging with high resolution spectroscopy, the exoplanet community is now using HCI to characterize exoplanets. With better understanding of the exoplanets currently seen and the recently imaged disks, a clearer picture of planet formation can be made.

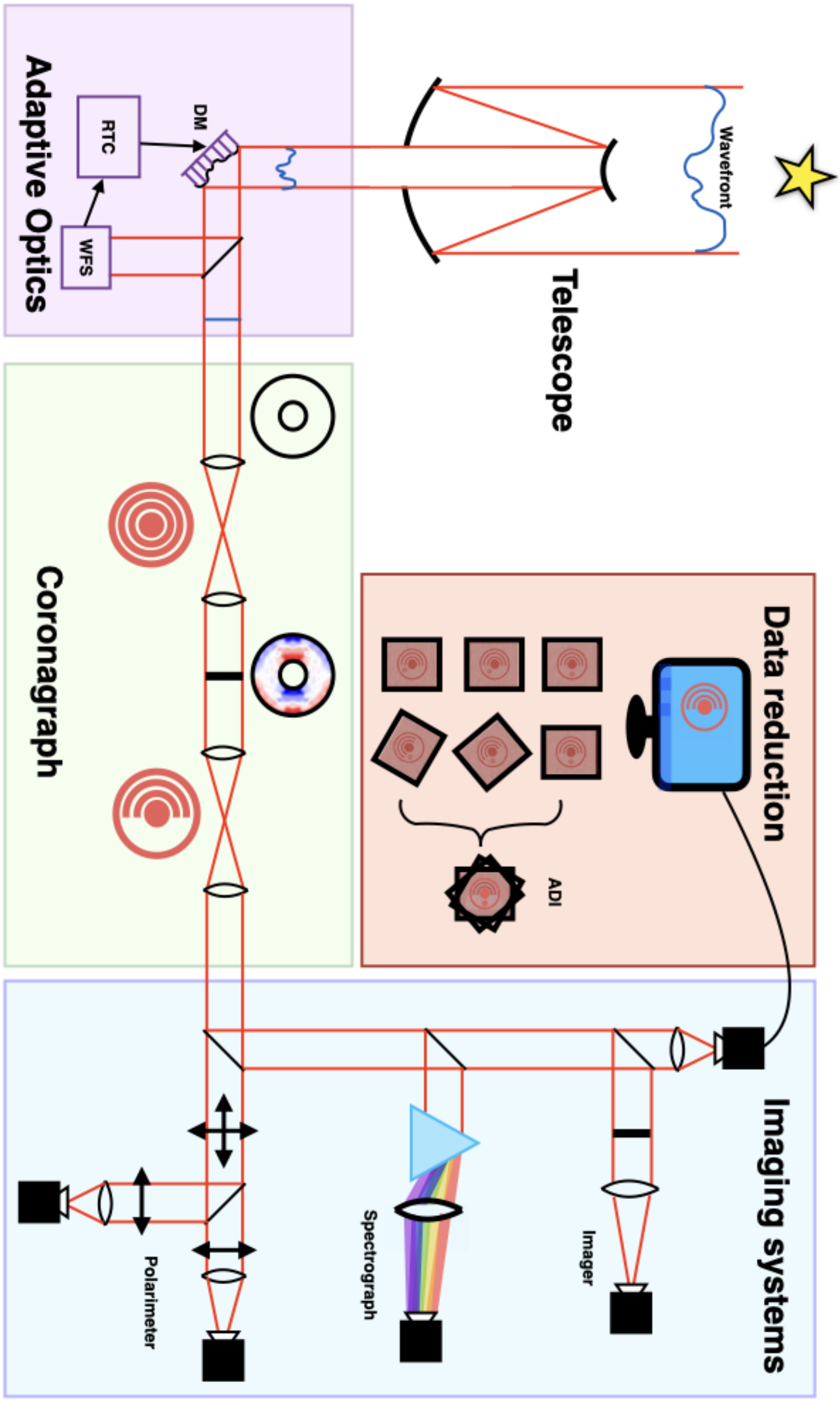

Figure 1.5: Schematic of an HCI system showing the four important components – adaptive optics, coronagraph, imaging systems, and data reduction – of the instrument. Image courtesy of David Doelman.

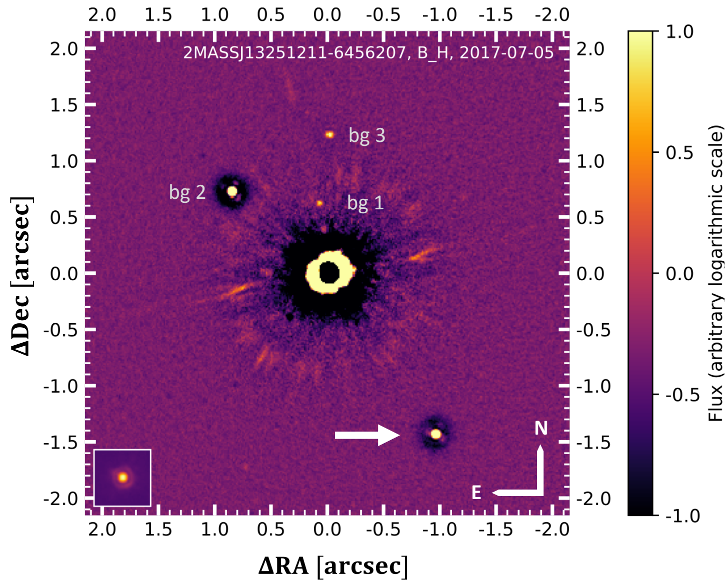

Figure 1.6: Reduced VLT/SPHERE H-band imaging data for TYC8998-760-1. The arrow indicates the far-out co-moving companion while the other objects are background objects (abbrev. bg) as seen by Bohn et al. (2019).

A schematic of an HCI system is shown in Figure 1.5. The extreme adaptive optics (XAO) system (see Section 1.3 for more details) removes aberrations due to atmospheric turbulence and other sources of error, in order to deliver the requisite spatial resolution. The corrected electric-field is relayed through a coronagraph, such as the vector-apodizing phase plate (vAPP) developed by Snik et al. (2012), to suppress the light of the host star over specified spatial frequencies. This creates a dark hole (often a ring) in the focal plane spanning from a prescribed inner working angle (iwa) to an outer working angle (owa). In Figure 1.6 there is a dark area in the centre of psf where the core has been blocked. There is then a halo of light in a butterfly shape (i.e., wind-driven halo, WDH, due to wind blowing turbulent patches across the telescope aperture; see Section 1.3.1) and then the dark ring starting at the iwa suppressing the star light out to the owa. At larger separations, exoplanets are revealed using data reduction techniques, such as angular differential imaging (ADI) developed by Marois, Lafreniere, et al. (2006). ADI relies on diversity introduced into a set of images taken in sequence by field rotation during the observation in order to reduce quasi-static aberrations (slowly changing aberrations). Finally, polarisation, spectroscopy, imaging, and focal plane wavefront sensing all further help to increase the achievable contrast of the system.

HCI challenges

Despite the discovery HCI systems have provided, there are many challenges associated with HCI, preventing the systems from being sensitive to small angular spatial separations (i.e., exoplanets that are either further away or have a small semi-major-axis, a). Currently, technological problems prevent HCI systems from achieving the necessary performance. Two major limiters of HCI systems are the unseen aberrations (by the XAO system) within an instrument's science path (e.g., non-common path aberrations) and the servo-lag error (i.e., the temporal error) Artigau et al. (2018). Removal of non-common path aberrations (NCPA; combination of chromatic errors and alignment and lens aberrations) can be done using focal-plane wavefront sensing techniques. Bos et al. (2019) reports on different methods applied to an HCI system using the vAPP to remove NCPA. **The servo-lag error, however, poses a significant challenge and requires a more in-depth look at the adaptive optics (AO) system.** The servo-lag error manifests itself as the WDH as described by Cantalloube, Por, et al. (2018) and occurs when the turbulence is moving faster than the XAO can handle. Figure 1.7 shows the focal plane with and without the WHD; it clearly shows how the region near the iwa becomes contaminated by speckles. From Cantalloube, Farley, et al. (2020), we know the conditions that cause the WDH at VLT/SPHERE occur $30-40\%$ of the time.

1.3 Adaptive Optics

An AO system provides the spatial resolution required for astronomical imaging with large telescopes. The diffraction limit of a telescope (and estimation of the angular

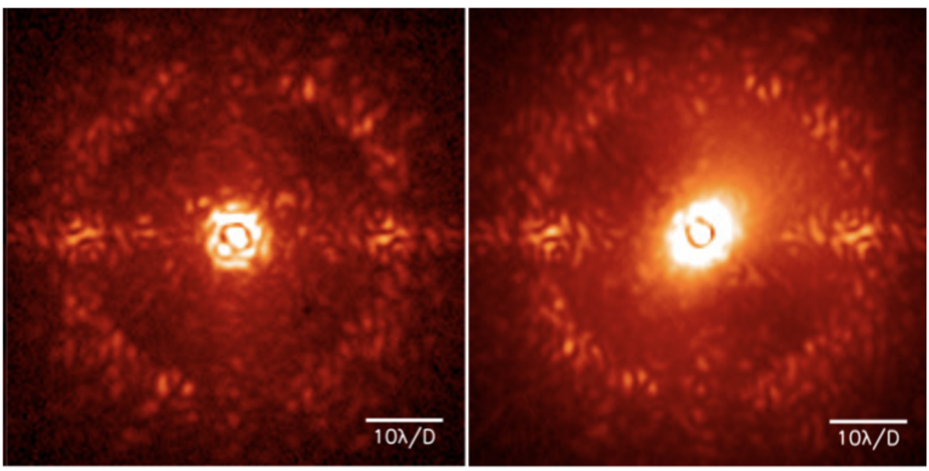

Figure 1.7: Focal plane images without (left) and with (right) the WDH for VLT/SPHERE. Taken from Cantalloube, Farley, et al. (2020).

resolution) is given by $\frac{\lambda}{D}$ with λ being the wavelength and D being the telescope diameter. As the diameter of the telescope gets larger, the resolution is greater. In the presence of turbulence, however, the diffraction limit becomes $\frac{\lambda}{r_0}$ with r_0 being the Fried parameter — the coherence length of turbulence — which has values of 10–15 cm for $\lambda = 500nm$ (Hardy, 1998) and $r_0 \propto \lambda^{\frac{6}{5}}$. Large ground-based telescopes, $D >> r_0$, are severely limited in terms of their angular resolution compared to what they could otherwise achieve if there was no atmosphere. AO corrects for the turbulence in real-time, limiting the impact of the turbulence, and delivering the resolution needed for the science goals of the instrument. An XAO system is an AO system that pushes the diffraction limit as close as possible to the theoretical value.

Figure 1.8 shows the different components of an AO (or XAO) system. The deformable mirror (DM) is a thin mirror (continuous or segmented) with actuators that allow for the shape of the mirror's surface to be deformed. The actuator mechanism can be, among others, voice coil based, or, more popular for XAO, micro-electro-mechanical systems (MEMS) based. The actuator type influences the packing density, the stroke, the linearity, coupling, response time, hysteresis, and creep of the DM; all important factors for the controller and maximum performance. The wavefront sensor (WFS) measures the phase component of the incoming electric-field for a given reference object in the field-of-view: the guide star. The WFS encodes the phase of the incoming wavefront in the flux measured by the WFS camera. Figure 1.8 shows a pyramid WFS which uses a pyramid-shaped optical component to perform a knife-edge test (see Goodwin and Wyant (2006) for details) in two dimensions, creating four images of the pupil plane that encode the local derivatives of the wavefront. From the local derivatives, the phase of the electric-field can be reconstructed (for more information see Kooten et al. (2017)). The WFS often senses in a different wavelength than the science path, using a beam splitter to provide as many photons as possible to both the WFS and the science focal plane to reduce the exposure time needed for a good SNR for both cameras. The real-time-computer (RTC) takes the information from the WFS camera and translates the signal to actuator commands for the DM. An AO system can operate in two different configurations: closed-loop (WFS measures the residual phase) or open-loop (WFS measures the full phase). Closed-loop configuration is most often used.

As mentioned above, an XAO system is the same as a basic AO system but with a larger number of degrees-of-freedom for a given field-of-view. An XAO system needs to deliver a high correction over a small field-of-view using an on-axis target as the guide star. This is done by making use of a high-order DM where the number of actuators is much greater ($> 2\times$) than an AO system for the same D and field-of-view. The XAO system is also required to run much faster, aiming for a WFS frame rate on the order of a couple of kiloHertz (kHz).

AO performance metrics and error terms

The Strehl ratio and variance of the phase are both used to describe the performance of an AO system. *Strehl ratio* (SR) is the ratio of the peak image intensity of the aberrated psf of a point source, compared to the maximum intensity of the idealised

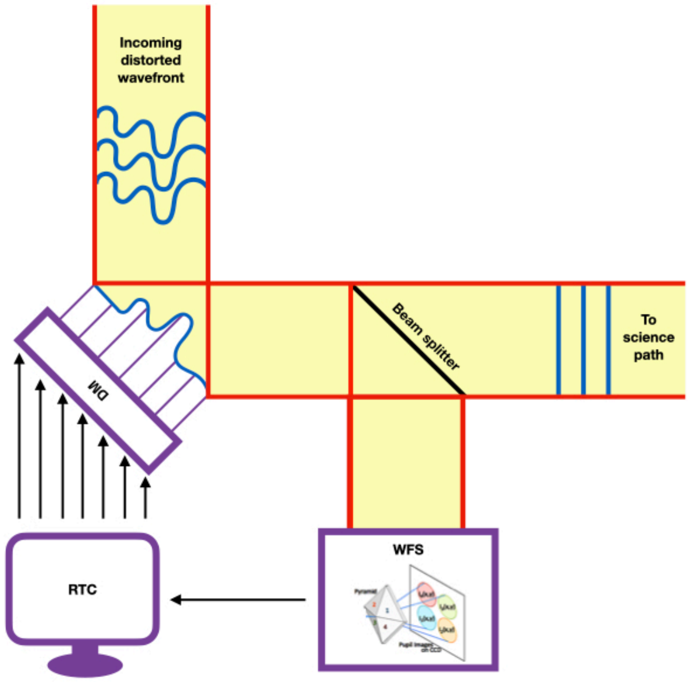

Figure 1.8: Schematic of an AO system in a closed-loop configuration. The incoming distorted phase of the electric-field is corrected by the DM. The corrected light then passes through a beam splitter where some of the light goes to the WFS where the residual wavefront error is sensed. The WFS sends the information to the RTC which calculates the commands to give to the DM.

optical system, which is limited only by the diffraction over the aperture. SR provides a measurement of the image quality and therefore how well an AO system corrects for atmospheric turbulence.

Standard AO systems typically minimise the phase variance of the wavefront instead of the SR. The post-AO phase variance is then a summation of different terms in the AO error budget. Errors from the WFS and DM are the fitting error (spatial under-sampling of the DM), aliasing error (not measuring high spatial frequencies and frequency folding of high spatial frequencies into low spatial frequencies due to WFS sampling), and measurement error (photon noise, read-out noise, etc for WFS). The system also has uncorrected atmospheric errors due to anisoplanatism, scintillation, diffractive effects, and differential refraction (for more information see Hardy, 1998). Finally, the AO system has a *temporal/servo-lag error* due to delays between camera read-out, DM response time, controller bandwidth, and the RTC computation time.

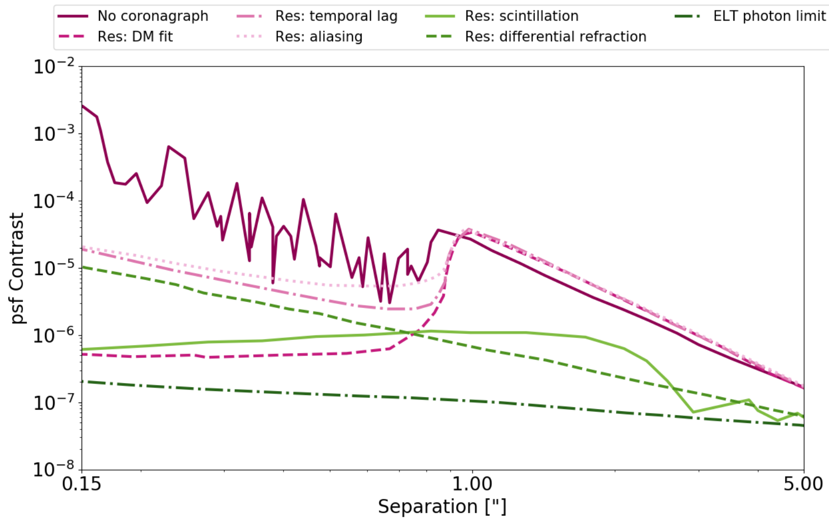

Figure 1.9: Contrast as a function of radial distance from the psf centre showing contributions of common residuals (Res.) in an XAO system based on VLT/SPHERE instrument and for reference the contrast floor for the Extremely Large Telescope (ELT). Differential refraction is a non-common path aberration. Scintillation is from amplitude errors which the XAO cannot correct. Figure taken from Pueyo (2018).

XAO's temporal error problem

Figure 1.9 shows the contribution of different error sources to the contrast as a function of radial separation for the VLT/SPHERE system (Beuzit et al., 2008). For an XAO system, the DM and WFS sampling can be increased to reduce the fitting error and aliasing error. The guide star in an XAO system is the central star (or host star that is being suppressed). The star is often bright enough that the WFS has a good SNR; since the guide star is on-axis, an XAO system does not suffer from anisoplanatism. Finally, the frame-rate of the WFS in many XAO systems is faster than 1 kHz with a delay of 2–4 WFS frames contributing to the temporal error. Note that the assumed operating frequency in Figure 1.9 is 1500 Hz – VLT/SPHERE runs at 1380 Hz and therefore the effect of the temporal error is underestimated. All of this results in the temporal error being a large source of error in an HCI system, limiting the contrast. In the following sections, we will further introduce the temporal error and its effect on an (X)AO system, including how the effect of the delay can be mitigated. **Mitigating the effect of the temporal delay is the main focus of this dissertation.**

1.3.1 AO Control and Disturbance rejection

Many AO control systems make use of very simple, but effective, control methods. Figure 1.10 is a block diagram of an AO system in a closed-loop configuration. This setup uses feedback to drive the system to the desired state. Note that an AO system

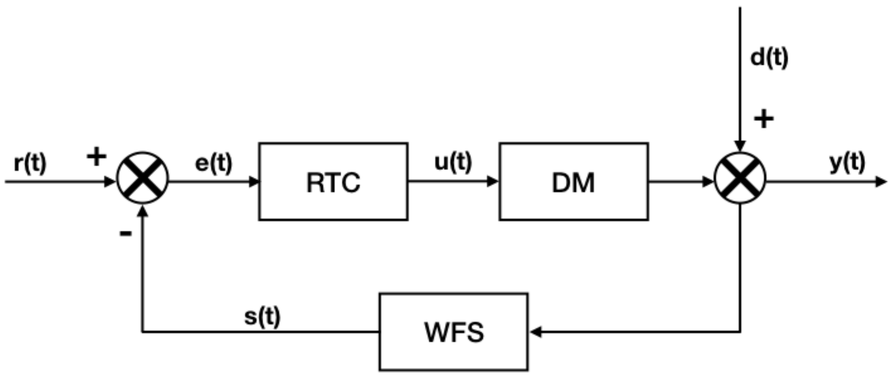

Figure 1.10: Block diagram of an AO system in closed-loop configuration. It shows the system plant as the DM, the WFS measures and feeds the RTC which calculates the control commands for the DM.

is a multi-input-multi-output system. In Figure 1.10 the system is provided a reference point ($r(t)$; either a flat wavefront or an offset to correct for NCPA). The RTC receives an error signal, $e(t)$, that informs the control law how far a recent correction was from $r(t)$. The RTC then calculates the updated commands, $u(t)$, according to the controller and sends these to the DM. The DM applies the correction, rejecting $d(t)$ (the input disturbance), and producing a corrected wavefront—$y(t)$—which is seen by the science camera and the WFS, allowing it to measure the residual input disturbance. Input disturbances are external processes that drive the system away from the desired state. In an AO system the input disturbance is a combination of atmospheric turbulence, telescope vibrations, and noise that introduce phase aberrations into the system. In this work we focus on atmospheric turbulence being the sole input disturbance.

$$u(t) = g \int_0^t e(\tau) d\tau \tag{1.1}$$

The control law used by many AO systems in closed-loop operation is an integral control law (integrator). An integrator action says that $u(t)$ is proportional to the integral of the error (in a discrete system: the sum of all previous errors) as given in Equation 1.1. The integral controller is sensitive to the magnitude and duration of the error. The gain, g, is chosen such that control bandwidth—how fast the system responds to the changing $e(t)$—is as high as possible while maintaining the stability of the system. In the case of an AO system, a g value close to unity is ideal for disturbance rejection when the plant dynamics are negligible. When the plant dynamics cannot be ignored, as in the case for a real-life AO system, g must be reduced in order to keep the system stable. Since the power spectral density (PSD) of turbulence is dominated by the low frequency components (see Section 1.3.1) and the integral controller has a high loop gain over this frequency range, reasonable performance is achieved for most conditions. An integrator properly tuned will therefore result in sustainable disturbance rejection and good correction for the system resulting in SR$= 30-50\%$ for regular AO systems or SR $> 90\%$ for XAO systems. The benefit of such a control law is that it performs reasonably well for an AO system subject to many different conditions with minimal or coarse tuning of the gain parameter. The integral controller does not, however, provide optimal control or guarantee control stability. For more in-depth background information on control for AO systems can be found in Roddier (1981) and Hardy (1998).

Describing Optical Aberrations

Ultimately, an AO controller aims to minimise the phase variance directly or indirectly. However, different formulations can be used to describe the aberrations seen by the system and change the mathematical representation of the system and controller. Within an AO system the aberrations can be described as by a zonal or modal basis. In the zonal representation, each actuator of the DM is controlled separately by the WFS signal conjugate to that by the area (zone) of the DM. For a modal representation, the aberrations are expressed as a linear combination of a spatial basis set (spanning the pupil) that best fit the WFS data. In AO, Zernike modes are often used to describe wavefront errors and are easy to understand from a user perspective (Noll, 1976). Furthermore, they are orthogonal over a circular aperture.

In the above discussion on control, we have made some important assumptions about the AO system including that the system is linear, continuous, and free of temporal delays. We, however, have also stated that the system does indeed have delays resulting in the servo-lag error (Hardy, 1998). In Figure 1.10, we can add a delay of Δt time steps such that the DM shape is a result of $u(t-\Delta t)$. The delay has an important effect for the system as the input disturbance (i.e., atmospheric turbulence) is not static but varies in time.

Atmospheric turbulence

The atmosphere can be thought of as a finite number of parallel layers of air that behave differently to one another (i.e., each with different wind speed and direction). Turbulence is caused by convection and/or shearing between the different layers. To completely understand the behaviour of turbulence the Navier-Stokes equations must be solved for the appropriate boundary conditions. In AO, however, a simplified approach is used to understand the statistical behaviour of optical turbulence.

Kolmogorov (1941) postulated that flows with high Reynolds numbers (i.e., those in which turbulence is dominant) are statistically isotropic and that the small (inner) scale of the energy cascade (the transfer of energy from large scales of motion to small scales of motion) is universal and uniquely determined by the kinematic viscosity and rate of energy dissipation. By knowing the large (outer) scale of the energy cascade, one could determine the spatial statistical behaviour of the turbulence between the inner and outer scales (the so-called inertial range). The idea is further

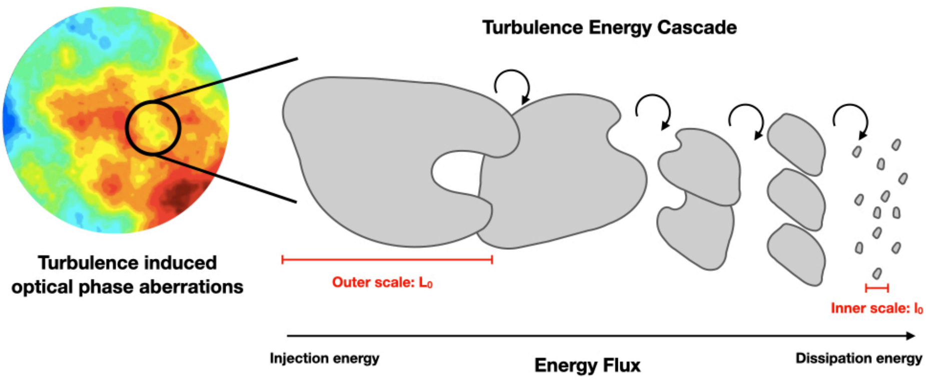

Figure 1.11: The turbulence energy cascade described by Kolmogorov (1941). In a turbulent flow energy is injected at the largest spatial scale (L_0) and cascades down into smaller and smaller scales until it dissipates at the smallest spatial scale, l_0. The spatial scales between these two limits are the main contributors to the optical phase aberrations seen above a telescope.

illustrated in Figure 1.11. Comparison of Kolmogorov's theory to experimental values has led to Kolmogorov's PSD. Currently, the von Kárman phase PSD (a modified Kolmogorov PSD) can be used to explain the spatial properties of observed optical turbulence, see Azoulay et al. (1988).

The modified von Kárman spatial PSD describing phase fluctuations due to atmosphere turbulence integrated for all heights is given by:

$$\Phi(k) = \frac{0.023}{r_0^{5/3}(k^2 + k_0^2)^{11/6}} e^{\frac{-k^2}{k_m^2}}$$
$$k_m = \frac{5.92}{l_0}$$
$$k_0 = \frac{2\pi}{L_0}$$

with l_0 and L_0 as the inner and outer scales in meters, respectively. With this equation, the spatial behavior of the phase can be determined by l_0, L_0, and r_0.

To further simplify the problem, the temporal behaviour of turbulence can be assumed to be the result of wind alone. According to Taylor's Frozen Flow hypothesis (Taylor, 1938), turbulent patches remain constant and are simply blown horizontally by the wind. In the case of a telescope aperture, temporal variations in turbulence at a given location are due to spatial variations being moved in time. Using this idea an expression of the temporal PSD is derived by Harrington and Welsh (1994), assuming the von Kárman spatial PSD. Assuming the inhomogeneities of the atmosphere remain fixed as it moves with a specific wind velocity (i.e., Frozen Flow), v, the single-sided and single-layer temporal PSD as a function of frequency, f, is given by:

$$W(f) = 0.033C_n^2\bar{k}^2hv^{5/3}(f^2 + \frac{k_0^2v^2}{4\pi^2})^{-4/3}$$

with h being the optical path length through the turbulence (e.g., for on-axis it would be the height of the layer), C_n^2 encoding the turbulence strength at that height, $\bar{k} = \frac{2\pi}{\lambda}$, and ignoring l_0. By integrating over all heights we can find a temporal PSD for the full turbulence above the telescope using $r_0 \propto (\int_0^\infty C_n^2(h)dh)^{-3/5}$

Non-stationary turbulence

The simplified description of optical phase variations due to atmospheric turbulence presented above assumes that the optical phase due to turbulence is a statistically stationary process (meaning the mean and variance do not change in time). While this assumption may be true over certain timescales or even at certain telescope locations, in reality atmospheric turbulence is a non-stationary process (Tokovinin and Travouillon, 2006) where the rate at which the mean and variance change is unknown and might differ throughout a night or from night to night. Using the above framework, a simple way of understanding what might be happening in real life is to imagine that the parameters of the von Kárman PSD vary in time. When this occurs, the optical phase fluctuations have non-stationary behaviour. Figure 1.12 illustrates

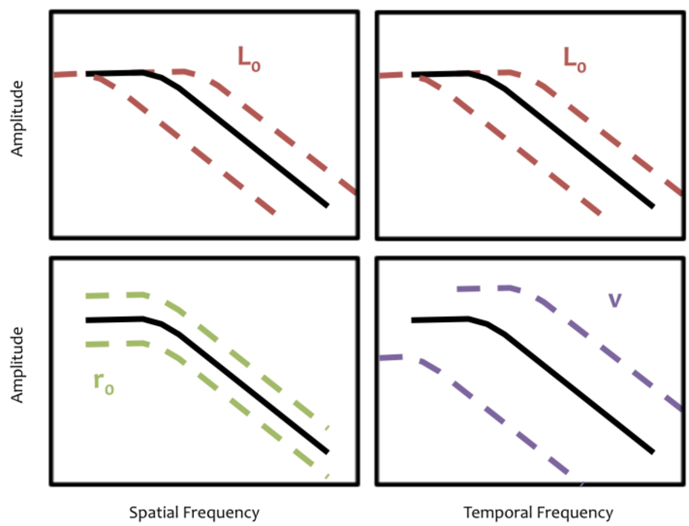

Figure 1.12: Sketch of the von Kárman PSD for spatial and temporal frequencies. The black line is a reference PSD while the dashed lines show how the PSD changes for the indicated parameters. The outer scale varies both the spatial and temporal PSD while the Fried parameter affects the spatial PSD and the wind speed affects the temporal PSD.

the effects v, r_0, and L_0 have on both the spatial and temporal PSDs. From a controller perspective, the changes in the temporal cut-off frequency are most important and this occurs when either v or L_0 change in time. L_0 also changes the spatial cut-off frequency. r_0 changes only the gain (amplitude) of the spatial PSD. The first step to understanding the impact of non-stationary turbulence on an XAO system is to determine how to model it and see the effects it has in simulation. Currently, the non-stationarity aspect of turbulence is observed through changes of the C_n^2 profile (integrating these profiles over all heights gives r_0) throughout a night as shown in Figure 1.13. These profiles, however, are estimated over a couple of minutes limiting the accuracy for which we can understand what the atmosphere is doing on shorter timescales as explained by Tokovinin and Kornilov (2007). In this dissertation we answer the question **how can we model non-stationary atmospheric turbulence phase fluctuations?**

Disturbance and the Servo-lag Error

In an HCI system one tangible manifestation of the servo-lag error is the WDH that appears as a butterfly pattern in the coronagraphic/science image (Cantalloube, Por, et al., 2018), see Figure 1.7. The WDH provides a visual example of how the servo-lag error limits the contrast at small angular separations. The WDH is the focal plane representation of the temporal error that is defined in the pupil plane. The impact of the error on the focal plane is directly related to the behavior of the turbulence. If the turbulence is evolving slower than the lag in the control system, the servo-lag has minimal impact and vice-versa. In other words, if the turbulence coherence time ($\tau = 0.314 r_0/v$) is shorter or close to the XAO lag time, the WDH appears in the

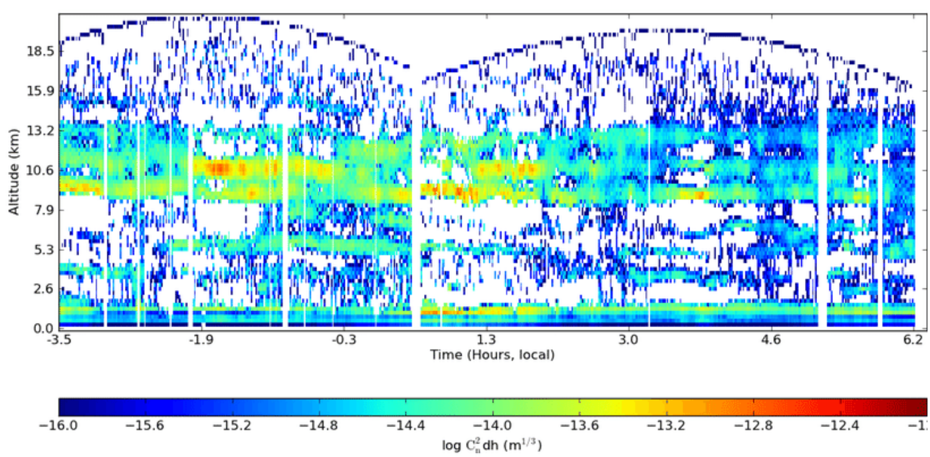

Figure 1.13: C_n^2 profiles taken by the Stereo-SCIDAR instrument on the Isaac Newton Telescope. The data, taken starting the night of 17 September 2014, shows a turbulent layer around 1 km and 3 separate layers between 9 and 13 km that all vary in strength throughout the night. Figure taken from Morris et al. (2014).

focal plane. The relation between τ, r_0, and therefore λ is one reason why AO is easier for longer wavelengths.

While an AO system minimises the phase variance, the metric that matters for an HCI system is the raw contrast. Even though the servo-lag error is relatively small and can be ignored for regular AO systems, it has a large impact on XAO systems as seen for observations (see Figure 1.7) and must therefore be addressed. One area of ongoing research is to verify how the non-corrected atmospheric turbulence affects the raw contrast and if it agrees theoretical expectations (e.g., Guyon, 2005; Cantalloube, Por, et al., 2018). This varies with a number of assumptions about the system especially the turbulence model as well as the controller behaviour. This leads to an important question, **how much contrast is lost by assuming stationary turbulence in the controller design when the turbulent conditions are in fact non-stationary?**

To improve the contrast at small angular separations, one can focus directly on minimising the effects of the servo-lag error. One simple solution is to minimise the delay in the XAO itself by running everything faster. However, hardware limits the maximum attainable speed of the DM. Further, by running the XAO faster, the system can become photon starved, even for bright targets. An alternative solution is to upgrade the XAO control system by implementing a new control algorithm. **One type of control algorithm that has been investigated in recent years is predictive control, which aims to predict the evolution of the atmosphere during the time between measurement and correction. This approach directly targets the servo-lag error and is a topic of this dissertation.**

Prediction and Control

During the time delay, the atmospheric turbulence evolves; resulting in a residual phase variance due to the difference in the current and measured wavefront phase. The first mention of prediction in AO literature was made by (Hardy, 1998). The idea of the traveling wave predictor was based on Frozen Flow and would compensate for the longer delays seen in initial AO systems. Since then, prediction has been implemented as a by-product of work in optimal control for various AO systems where the necessary SR is much lower than that required in XAO and the servo-lag error is not the dominant error term in the system. Since then, data-driven techniques have been investigated for the purpose of prediction for XAO systems.

Optimal Control One can determine the optimal control law for a dynamical system described by a set of equations. The control problem is defined by a cost function that is a function of the states (e.g., measured zonal modes that describe the phase distortion) and control variables (e.g., DM actuators' values) of the system. The control law is then determined by minimising a chosen cost function. Different cost functions result in different optimal control laws. Some of the important work done using the optimal control framework is highlighted below.

The linear-quadratic regulator (LQR) is a controller that minimises a quadratic cost function for a linear system with feedback. When the system is subject to Gaussian noise, the feedback control law becomes the linear-quadratic-Gaussian (LQG) controller making use of the Kalman filter. One challenge of LQG control is that it requires an accurate model of the plant (DM and WFS) as well as the input disturbance (turbulence). In a series of papers (see Looze (2006), Looze (2008), and Looze (2009)) the LQG controller is studied for AO systems. Many different assumptions have been explored in modelling the plant, ranging from ignoring the DM dynamics to full modelling of the DM based on laboratory measurements. For the input disturbance, LQG can do a good job rejecting telescope vibrations that are easy to accurately model (Sivo et al., 2014). However, extending the model to reject atmospheric turbulence has proven more difficult. The main trouble arises from estimating a model for atmospheric turbulence in a finite (manageable size) state-based representation that accurately represents the turbulence. As such, in the literature an auto-regressive model of order one is often used to describe atmospheric turbulence with an understanding that it can be expanded to include higher order terms if necessary (Le Roux et al., 2004). In theory, once the temporal effects are included in the controller, the Kalman filter using this atmospheric model performs prediction at each time step. To date there has been limited success on-sky using the LQG controller for full atmospheric turbulence rejection. It is also important to note that LQG optimality does not automatically ensure good robustness. The robust stability of the closed-loop system must be checked separately after the LQG controller has been designed; this requires substantial on-sky testing for verification.

By making slight changes to the cost function of the LQG controller one can form the H2 optimal controller. On-sky tests by Doelman et al. (2011) show a reduction in the temporal error for tip-tilt control. In designing this controller two different approaches for modelling the atmospheric disturbance were explored by Hinnen et al. (2007). First, using a theoretical turbulence spectrum and, second, using the open-loop WFS data (WFS directly measures the full turbulence as it is placed before the DM) to determine the disturbance. The work demonstrates the importance of proper modelling of the atmospheric disturbance to have an accurate enough model for optimal control to perform well. Once again due to the model of the system having a temporal delay, the optimal control law, by design, performs prediction as part of the control law.

Linear Data-Driven Prediction for XAO Current work on linear prediction in XAO primarily focuses on the prediction of atmospheric turbulence as a step before the controller. Therefore, the control law is unaware of the existence or influence of the prediction step. Specifically, the prediction algorithms are chosen to be data-driven, and learn online as modelling the atmosphere's behaviour to the accuracy needed for XAO systems has proven to be difficult if not impossible.

The prediction is performed by estimating the pseudo-open loop phase (full turbulence phase calculated from knowing the WFS values and the DM shape; instead of phase can use slopes, or modes instead) and applying a predictive filter before the control algorithm. This approach allows for a system architecture that can turn prediction on and off with minimal effect on the control loop. Furthermore, one can test the predictability of turbulence and not focus on the behaviour of the control loop itself. A similar structure has been implemented using the CACAO RTC (Guyon, Sevin, et al. (2018)). Empirical orthogonal functions (EOF) is a data-driven predictor that minimises the phase variance. Implemented on SCExAO (an HCI instrument at the Subaru telescope in Hawaii), Guyon, Sevin, et al. (2018) have demonstrated that EOF improves the standard deviation of the psf over a set of images. However, the improvement is less than expected from initial simulations by Guyon and Males (2017). Prediction might also perform differently at other observing sites where the turbulence behaves differently. This leads me to ask **how does prediction perform for the VLT/SPHERE in Paranal?**

Similar methods to EOF minimise the same cost function as EOF but with a different evaluation of the necessary covariance functions, including the prediction done in this work. A posteriori tests by Jensen-Clem et al. (2019), using AO telemetry, show an average factor of 2.6 improvement for contrast for separations from 0 to $10\lambda/D$. All these tests have shown that improvement expected from prediction is not seen in reality. We therefore ask the following questions: **what improvement is expected from prediction when assuming non-stationary turbulence, and how does linear data-driven prediction behave under different input disturbances?**

1.4 In this Dissertation

In the above sections, we introduce and motivate the 6 main questions addressed in this dissertation:

1. What type of astronomical objects could be the cause of these brightening events in the Kepler database?
2. How can we model non-stationary atmospheric turbulence phase fluctuations?
3. Given that turbulence is non-stationary, how much contrast is lost by assuming stationary turbulence in the controller design?
4. How does linear data-driven prediction behave under different input disturbances?
5. What improvement is expected from prediction when assuming non-stationary turbulence?
6. How does prediction perform for the VLT/SPHERE in Paranal?

In Chapter 2 of this dissertation, we take a closer look at Q1. We investigate two possible mechanisms to explain the observed light curves, namely: forward scattering from an optically thin dust cloud, and tidal interactions from a close binary star system.

The subsequent chapters transition to focus on HCI and control: from improving atmospheric turbulence modelling, seeing the effects of this on contrast and linear prediction, and finally studying how prediction performs with real atmospheric optical phase aberrations. Chapter 3 introduces a linear data-driven predictor and assumes simple cases of non-stationary turbulence (such as wind gusts and varying

r_0 based off similar data shown in Figure 1.13) to show that changes to the disturbance model can have a large effect on prediction, thereby briefly looking at Q2 and Q4. These results lead to the work presented in Chapter 4. In this chapter we form a more realistic non-stationary model of atmospheric turbulence using Thirty Meter Telescope (TMT) site testing data to form a wind model allowing for the modelling of non-stationary turbulence, addressing Q2. Using this model, we study how much contrast is lost for an ideal integrator, assuming either constant wind or varying wind speed, in order to address Q3. To investigate Q4, we utilise the non-stationary model of atmospheric-turbulence-induced phase, and apply a linear data-driven predictor in Chapter 5. We then quantify the improvement expected, answering Q5. In Chapter 6, we verify the answer to Q5, and answer Q6, while studying prediction on VLT/SPHERE testing prediction under 27 different atmospheric conditions.

In summary, the main conclusions of this dissertation are:

- **For the 8 WOI identified in the Kepler data both forward scattering and highly elliptical binary star system models can explain the observed brightening in the light curves.**
- **Under time varying turbulence due to changing wind speed, an XAO loses performance.** For a standard integral controller, sub-second wind speed fluctuations affect contrast by less than 5%, however, wind speed changes on longer timescales led to a much larger loss in contrast than predicted by the fundamental limitations. An XAO system needs to track the wind speed at rates faster than 2 minutes for the given wind statistics on Mauna Kea. A linear data-driven predictor will also lose performance due to the inability to track the varying statistics compared to the optimal implementation of the same predictor with infinite tracking capabilities.
- **For VLT/SPHERE, a linear data-driven predictor results in an improvement of performance.** For the 27 various observing conditions studied, the XAO correction is more reliable and consistent. The optical turbulence as seen by VLT/SPHERE is also time-invariant. Therefore, the temporal regressors of the predictor have a larger impact on the performance than the spatial regressors. A batch temporal-only predictor for the VLT/SPHERE is therefore recommended to reduce the servo-lag error.

1.5 Outlook

With the end of the Kepler mission and the start of the TESS era in precision photometry, more and more light curves are being obtained for a fast portion of the sky. In the last few years, new methods have also been employed for searching through databases looking for new signals and outliers. It is important to look at these objects and model the physics behind them, as done in this dissertation. These signals could indeed be an exoplanet/proto-planetary disk system in configurations previously not detected, thereby providing new insights. Finally, for the objects in Chapter 2 follow-up observations will be necessary to fully understand what is truly occurring to create the observed Kepler light curves and distinguish which model is responsible for the increase in flux.

As HCI systems are being built for the next generation of large telescopes it is necessary to fully understand the relation between atmospheric turbulence, predictive control, and contrast. To do this, it is essential for the community to first understand the main differences in the performance of linear prediction at Hawaii, Paranal, and other observatory locations. This requires a good understanding of the telescope, instrument and the full implementation of the controller, as well as the atmosphere above the telescope. At specific sites, different predictive control schemes might be better suited for a given site or telescope due to the input disturbances. More specifically, we find in Chapter 5 that how well the predictor performs is related to L_0 and the telescope diameter. Especially for the extremely large telescopes, it is important to truly know what possible values for L_0 are and how it evolves in time. Furthermore, in Chapter 6 we find evidence that input disturbances other than atmospheric turbulence (e.g., telescope vibrations) might have a large effect on the controller and therefore final contrast; this is different from originally thought and must be considered for future HCI systems. Finally, the final raw contrast is the critical performance index for HCI. Investigating the effects of prediction on contrast for different types of coronagraphs, and determining whether predictive control can be used to directly optimise the raw contrast (either over a part of the field-of-view or the entire focal plane) is an interesting research direction.

Another crucial step for AO control, especially XAO control, is to have flexible instruments and telescope facilities to allow for the testing of new control schemes to further develop them and provide the required performance. Being able to test controllers in real-life situations under a variety of conditions is invaluable. With access to these types of testing, different control schemes can more readily be explored such as data-driven optimal control or model predictive control. By looking into the topics outlined above, the control community can provide the best performance for HCI systems such that the contrast at smaller angular resolutions will allow for the imaging, and subsequent characterisation, for far away and close-in exoplanets.

References

Advanced School on Exoplanetary Science (1st : 2015 : Vietri sul Mare, Italy), Valerio Bozza, Luigi (Research scientist) Mancini, and Alessandro Sozzetti (2016). "Methods of detecting exoplanets : 1st Advanced School on Exoplanetary Science". In:

Ahlers, John P. et al. (Jan. 2020). "Gravity-darkening Analysis of the Misaligned Hot Jupiter MASCARA-4 b". In: *The Astrophysical Journal* 888.2, p. 63.

Artigau, Etienne et al. (Aug. 2018). "Direct Imaging in Reflected Light: Characterization of Older, Temperate Exoplanets With 30-m Telescopes". In: *arXiv e-prints*, arXiv:1808.09632.

Avenhaus, Henning et al. (Aug. 2018). "Disks around T Tauri Stars with SPHERE (DARTTS-S). I. SPHERE/IRDIS Polarimetric Imaging of Eight Prominent T Tauri Disks". In: *The Astrophysical Journal* 863.1, p. 44.

Azoulay, E, V Thiermann, A Jetter, A Kohnle, and Z Azar (Oct. 1988). “Optical measurement of the inner scale of turbulence”. In: *Journal of Physics D: Applied Physics* 21.10S, S41–S44.

Beuzit, J.-L. et al. (July 2008). “SPHERE: a ’Planet Finder’ instrument for the VLT”. In: *Proc.SPIE* 7014, p. 701418.

Bohn, A J et al. (Dec. 2019). “The Young Suns Exoplanet Survey: Detection of a wide-orbit planetary-mass companion to a solar-type Sco-Cen member”. In: *Monthly Notices of the Royal Astronomical Society* 492.1, pp. 431–443.

Borucki, William J. et al. (2010). “Kepler Planet-Detection Mission: Introduction and First Results”. In: *Science* 327.5968, pp. 977–980.

Bos, S. P., D. S. Doelman, J. Lozi, O. Guyon, C. U. Keller, K. L. Miller, N. Jovanovic, F. Martinache, and F. Snik (Nov. 2019). “Focal-plane wavefront sensing with the vector-Apodizing Phase Plate”. In: *Astronomy & Astrophysics* 632, A48.

Campbell, Bruce, G. A. H. Walker, and S. Yang (Aug. 1988). “A Search for Substellar Companions to Solar-type Stars”. In: *The Astrophysical Journal* 331, p. 902.

Cantalloube, F., E. H. Por, et al. (2018). “Origin of the asymmetry of the wind driven halo observed in high-contrast images”. In: *Astronomy & Astrophysics* 620, p. L10.

Cantalloube, Faustine, Ollie Farley, et al. (2020). *The wind-driven halo in high-contrast images I: analysis from the focal plane images of SPHERE*.

Charbonneau, D., T. M. Brown, D.W. Latham, and M. Mayor (Jan. 2000). “Detection of Planetary Transits Across a Sun-like Star”. In: *The Astrophysical Journall* 529.1, pp. L45–L48.

Charbonneau, D., T. M. Brown, R. W. Noyes, and R. L. Gilliland (Mar. 2002). “Detection of an Extrasolar Planet Atmosphere”. In: *The Astrophysical Journal* 568.1, pp. 377–384.

Doelman, N., R. Fraanje, and R. den Breeje (2011). “Real-sky adaptive optics experiments on optimal control of tip-tilt modes”. In: *2nd Conference on Adaptive Optics for Extremely Large Telescopes* 1.1.

Dorval, P. et al. (Mar. 2020). “MASCARA-4 b/bRing-1 b: A retrograde hot Jupiter around a bright A-type star”. In: *Astronomy & Astrophysics* 635, A60.

Goodwin, E.P. and J.C. Wyant (2006). *Field Guide to Interferometric Optical Testing*. Field Guide Series. SPIE.

Guyon, O. and J. Males (July 2017). “Adaptive Optics Predictive Control with Empirical Orthogonal Functions (EOFs)”. In: *ArXiv e-prints*.

Guyon, Olivier (Aug. 2005). “Limits of Adaptive Optics for High-Contrast Imaging”. In: *The Astrophysical Journal* 629.1, pp. 592–614.

Guyon, Olivier, Arnaud Sevin, et al. (2018). “The compute and control for adaptive optics (CACAO) real-time control software package”. In: *Adaptive Optics Systems VI*. Ed. by Laird M. Close, Laura Schreiber, and Dirk Schmidt. Vol. 10703. International Society for Optics and Photonics. SPIE, pp. 469–480.

Hardy, J. W. (1998). “Adaptive Optics for Astronomical Telescopes”. In: *Oxford University Press Jul 1998*.

Harrington, Patrick M. and Byron M. Welsh (1994). “Frequency-domain analysis of an adaptive optical system’s temporal response”. In: *Optical Engineering* 33.7, pp. 2336–2342.

Hatzes, Artie P., William D. Cochran, Michael Endl, Barbara McArthur, Diane B. Paulson, Gordon A. H. Walker, Bruce Campbell, and Stephenson Yang (Dec. 2003). "A Planetary Companion to γ Cephei A". In: *The Astrophysical Journal* 599.2, pp. 1383–1394.

Hinnen, Karel, Michel Verhaegen, and Niek Doelman (June 2007). "Exploiting the spatiotemporal correlation in adaptive optics using data-driven H2-optimal control". In: *J. Opt. Soc. Am. A* 24.6, pp. 1714–1725.

Jensen-Clem, Rebecca, Charlotte Z. Bond, Sylvain Cetre, Eden McEwen, Peter Wizinowich, Sam Ragland, Dimitri Mawet, and James Graham (2019). "Demonstrating predictive wavefront control with the Keck II near-infrared pyramid wavefront sensor". In: *Techniques and Instrumentation for Detection of Exoplanets IX*. Ed. by Stuart B. Shaklan. Vol. 11117. International Society for Optics and Photonics. SPIE, pp. 275–284.

Kolmogorov, A. (Jan. 1941). "The Local Structure of Turbulence in Incompressible Viscous Fluid for Very Large Reynolds' Numbers". In: *Akademiia Nauk SSSR Doklady* 30, pp. 301–305.

Kooten, Maaike van, Jean Pierre Veran, and Colin Bradley (2017). "Alternative pyramid wavefront sensors". In: *Journal of Astronomical Telescopes, Instruments, and Systems* 3.2, p. 029001.

Le Roux, B., R. Ragazzoni, C. Arcidiacono, J.-M. Conan, C. Kulcsar, and H.-F. Raynaud (Oct. 2004). "Kalman-filter-based optimal control law for star-oriented and layer-oriented multiconjugate adaptive optics". In: *Proc.SPIE* 5490, pp. 1336–1346.

Lesage, A.-L., J. F. P. Spronck, R. Stuik, F. Bettonvil, D. Pollaco, and I. A. G. Snellen (2014). "MASCARA: the multi-site all-sky CAameRA: concept and first results". In: *Ground-based and Airborne Telescopes V*. Ed. by Larry M. Stepp, Roberto Gilmozzi, and Helen J. Hall. Vol. 9145. International Society for Optics and Photonics. SPIE, pp. 402–409.

Looze, D. P. (July 2008). "Structure of a hybrid signal LQG controller for adaptive optics". In: *Adaptive Optics Systems*. Vol. 7015. Proceedings SPIE, p. 701536.

Looze, Douglas P. (Mar. 2006). "Minimum variance control structure for adaptive optics systems". In: *J. Opt. Soc. Am. A* 23.3, pp. 603–612.

— (Jan. 2009). "Linear-quadratic-Gaussian control for adaptive optics systems using a hybrid model". In: *J. Opt. Soc. Am. A* 26.1, pp. 1–9.

Marois, C., D. Lafreniere, R. Doyon, B. Macintosh, and D. Nadeau (Apr. 2006). "Angular Differential Imaging: A Powerful High-Contrast Imaging Technique". In: *The Astrophysical Journal* 641.1, pp. 556–564.

Marois, C., B. Macintosh, T. Barman, B. Zuckerman, I. Song, J. Patience, D. Lafreniere, and R. Doyon (2008). "Direct Imaging of Multiple Planets Orbiting the Star HR 8799". In: 322.5906, pp. 1348–1352.

Mayor, M., S. Udry, D. Naef, F. Pepe, D. Queloz, N. C. Santos, and Burnet, M. (2004). "The CORALIE survey for southern extra-solar planets*** - XII. Orbital solutions for 16 extra-solar planets discovered with CORALIE". In: *Astronomy & Astrophysics* 415.1, pp. 391–402.

Mayor, Michel and Didier Queloz (1995). "A Jupiter-mass companion to a solar-type star". In: *Nature* 378.6555, pp. 355–359.

Morris, Tim et al. (July 2014). "CANARY phase B: on-sky open-loop tomographic LGS AO results". In: vol. 9148, p. 91481I. DOI: 10.1117/12.2056279.

Noll, Robert J. (Mar. 1976). "Zernike polynomials and atmospheric turbulence∗". In: *J. Opt. Soc. Am.* 66.3, pp. 207–211.

Pueyo, Laurent (2018). "Direct Imaging as a Detection Technique for Exoplanets". In: p. 10.

Ricker, George R. et al. (Jan. 2015). "Transiting Exoplanet Survey Satellite (TESS)". In: *Journal of Astronomical Telescopes, Instruments, and Systems* 1, p. 014003.

Roddier, F. (Jan. 1981). "The effects of atmospheric turbulence in optical astronomy". In: *Progess in Optics* 19, pp. 281–376.

Sissa, E. et al. (2018). "New disk discovered with VLT/SPHERE around the M star GSC 07396-00759". In: *Astronomy & Astrophysics* 613, p. L6.

Sivo, Gaetano et al. (Sept. 2014). "First on-sky SCAO validation of full LQG control with vibration mitigation on the CANARY pathfinder". In: *Opt. Express* 22.19, pp. 23565–23591.

Snellen, Ignas A. G., Remco J. de Kok, Ernst J. W. de Mooij, and Simon Albrecht (June 2010). "The orbital motion, absolute mass and high-altitude winds of exoplanet HD209458b". In: *Nature* 465.7301, pp. 1049–1051.

Snik, Frans, Gilles Otten, Matthew Kenworthy, Matthew Miskiewicz, Michael Escuti, Christopher Packham, and Johanan Codona (Sept. 2012). "The vector-APP: a broadband apodizing phase plate that yields complementary PSFs". In: *Modern Technologies in Space- and Ground-based Telescopes and Instrumentation II*.

Taylor, Geoffrey Ingram (1938). "Production and dissipation of vorticity in a turbulent fluid". In: *Proceedings of the Royal Society of London. Series A - Mathematical and Physical Sciences* 164.916, pp. 15–23.

Tokovinin, A. and V. Kornilov (Oct. 2007). "Accurate seeing measurements with MASS and DIMM". In: *Monthly Notices of the Royal Astronomical Society* 381.3, pp. 1179–1189.

Tokovinin, A. and T. Travouillon (Feb. 2006). "Model of optical turbulence profile at Cerro Pachón". In: *Monthly Notices of the RAS* 365.4, pp. 1235–1242.

Wheeler, Adam and David Kipping (Mar. 2019). "The weird detector: flagging periodic, coherent signals of arbitrary shape in time-series photometry". In: *Monthly Notices of the Royal Astronomical Society* 485.4, pp. 5498–5510.

Wolszczan, A. and D. A. Frail (1992). "A planetary system around the millisecond pulsar PSR1257 + 12". In: *Nature* 355.6356, pp. 145–147.

Zurlo, A. et al. (2016). "First light of the VLT planet finder SPHERE - III. New spectrophotometry and astrometry of the HR9 exoplanetary system". In: *Astronomy & Astrophysics* 587, A57.